LETTER

doi:10.1038/nature10956

The BAH domain of ORC1 links H4K20me2 to DNA replication licensing and Meier–Gorlin syndrome

Alex J. Kuo[1]*, Jikui Song[2]†*, Peggie Cheung[1]*, Satoko Ishibe-Murakami[2], Sayumi Yamazoe[3], James K. Chen[3], Dinshaw J. Patel[2] & Or Gozani[1]

The recognition of distinctly modified histones by specialized 'effector' proteins constitutes a key mechanism for transducing molecular events at chromatin to biological outcomes[1]. Effector proteins influence DNA-templated processes, including transcription, DNA recombination and DNA repair; however, no effector functions have yet been identified within the mammalian machinery that regulate DNA replication. Here we show that ORC1—a component of ORC (origin of replication complex), which mediates pre-DNA replication licensing[2]—contains a bromo adjacent homology (BAH) domain that specifically recognizes histone H4 dimethylated at lysine 20 (H4K20me2). Recognition of H4K20me2 is a property common to BAH domains present within diverse metazoan ORC1 proteins. Structural studies reveal that the specificity of the BAH domain for H4K20me2 is mediated by a dynamic aromatic dimethyl-lysine-binding cage and multiple intermolecular contacts involving the bound peptide. H4K20me2 is enriched at replication origins, and abrogating ORC1 recognition of H4K20me2 in cells impairs ORC1 occupancy at replication origins, ORC chromatin loading and cell-cycle progression. Mutation of the ORC1 BAH domain has been implicated in the aetiology of Meier–Gorlin syndrome (MGS)[3,4], a form of primordial dwarfism[5], and ORC1 depletion in zebrafish results in an MGS-like phenotype[4]. We find that wild-type human ORC1, but not ORC1–H4K20me2-binding mutants, rescues the growth retardation of *orc1* morphants. Moreover, zebrafish depleted of H4K20me2 have diminished body size, mirroring the phenotype of *orc1* morphants. Together, our results identify the BAH domain as a novel methyl-lysine-binding module, thereby establishing the first direct link between histone methylation and the metazoan DNA replication machinery, and defining a pivotal aetiological role for the canonical H4K20me2 mark, via ORC1, in primordial dwarfism.

The identification of protein modules that recognize the broad spectrum of modifications present on histone proteins is critical for understanding how chromatin dynamics influence fundamental nuclear processes[6]. The BAH domain is an evolutionarily conserved chromatin-associated motif[7]. In budding yeast, the BAH domain of the silencing regulator Sir3 was shown to be a nucleosome-binding domain[8–10], suggesting that other BAH domains might function as chromatin-effector modules. To test this hypothesis, we screened several BAH domains from yeast and human for binding activity on peptide microarrays containing 82 modified and unmodified histone peptides, including 54 uniquely methylated peptides (Supplementary Fig. 1)[11]. The BAH domain of human ORC1 (ref. 12) (hORC1$_{BAH}$: amino acids 1–185) bound with high specificity to H4K20me2 peptides (Fig. 1a). In peptide pull-down assays, hORC1$_{BAH}$ bound H4K20me2 peptides, but did not interact with several other dimethylated histone peptides (Fig. 1b). In addition, hORC1$_{BAH}$ did not interact with unmodified H4 peptide, and showed a strong preference for H4K20me2 over H4K20me1 or H4K20me3 (Fig. 1c). Quantification of the interaction by isothermal titration calorimetry (ITC) demonstrated that hORC1$_{BAH}$ bound to H4(14–25)K20me2 peptides with a dissociation constant (K_d) of 5.2 μM, whereas monomethylation and trimethylation at K20 reduced the binding affinity fivefold (K_d = 24.8 μM) and eightfold (K_d = 40.0 μM), respectively (Fig. 1d). Finally, hORC1$_{BAH}$ bound to full-length H4K20me2 that is present in bulk-purified histones (Fig. 1e). Together, these *in vitro* results demonstrate that hORC1$_{BAH}$ binds with high specificity and affinity to H4K20me2.

ORC1 is an evolutionarily conserved protein, found in virtually all eukaryotes[2,12]. As shown in Fig. 1f, H4K20me2 recognition is a common activity of BAH domains of ORC1 from several different metazoans. In contrast, the BAH domains of ORC1 from yeast *Saccharomyces cerevisiae* (scORC1$_{BAH}$) and *Schizosaccharomyces pombe* lack H4K20me2-binding activity. In both of these yeast species, it is known that ORC binds directly to DNA sequences at origins of replication, whereas in metazoans, chromatin has a more significant role in directing ORC to replication origins[2,13,14].

To understand the molecular basis of the ORC1 BAH domain recognition of H4K20me2, the crystal structure of the complex between the H4(14–25)K20me2 peptide and the BAH domain of mouse ORC1(9–170) (mORC1$_{BAH}$) was solved at 1.95 Å resolution (Fig. 2a; crystallization statistics in Supplementary Table 1). mORC1$_{BAH}$ adopts a characteristic BAH-domain fold (Fig. 2a), as first reported for the scORC1$_{BAH}$[15]. Complex formation between H4(14–25)K20me2 and mORC1$_{BAH}$ is mediated by van der Waals contacts, hydrogen bonding and electrostatic interactions (Fig. 2b, c). The dimethylammonium group of H4K20me2 is anchored by cation–π interactions with the side chains of an aromatic cage located at the mORC1$_{BAH}$ surface and composed of Tyr 63, Trp 87, Tyr 114 and Trp 119, and the dimethylammonium proton is hydrogen bonded to the side chain of Glu 93 (Fig. 2d), similar to H4K20me2 bound to the 53BP1 Tudor domain[16] (Supplementary Fig. 2). The aromatic cage in mORC1$_{BAH}$ is absent in the published structure of scORC1$_{BAH}$ (Supplementary Fig. 3)[15], explaining why scORC1$_{BAH}$ does not bind H4K20me2 (Fig. 1f).

The preference of hORC1$_{BAH}$ for H4K20me2 over its me1/3 counterparts (see Fig. 1c) probably reflects the contribution from the hydrogen bond formed between the dimethylammonium proton and the side-chain carboxylate of Glu 93 (Fig. 2c). Indeed, previous studies demonstrated that a single Tyr-to-Glu substitution within an otherwise aromatic cage of the bromodomain and PHD domain transcription factor (BPTF) plant homeo domain (PHD) finger reverses the binding preference from trimethyl- to dimethyl-lysine[17]. Engineering a binding preference for H4K20me1 would probably require incorporation of a second carboxylate group to line the aromatic cage of hORC1$_{BAH}$ and facilitate hydrogen-bond formation with both monomethylammonium protons. The high degree of specificity of mORC1$_{BAH}$ for the sequence surrounding H4K20 is conferred by a series of intermolecular

[1]Department of Biology, Stanford University, Stanford, California 94305, USA. [2]Structural Biology Program, Memorial Sloan-Kettering Cancer Center, New York, New York 10065, USA. [3]Department of Chemical and Systems Biology, Stanford School of Medicine, Stanford, California 94305, USA. †Present address: Department of Biochemistry, University of California, Riverside, California 92521, USA. *These authors contributed equally to this work.

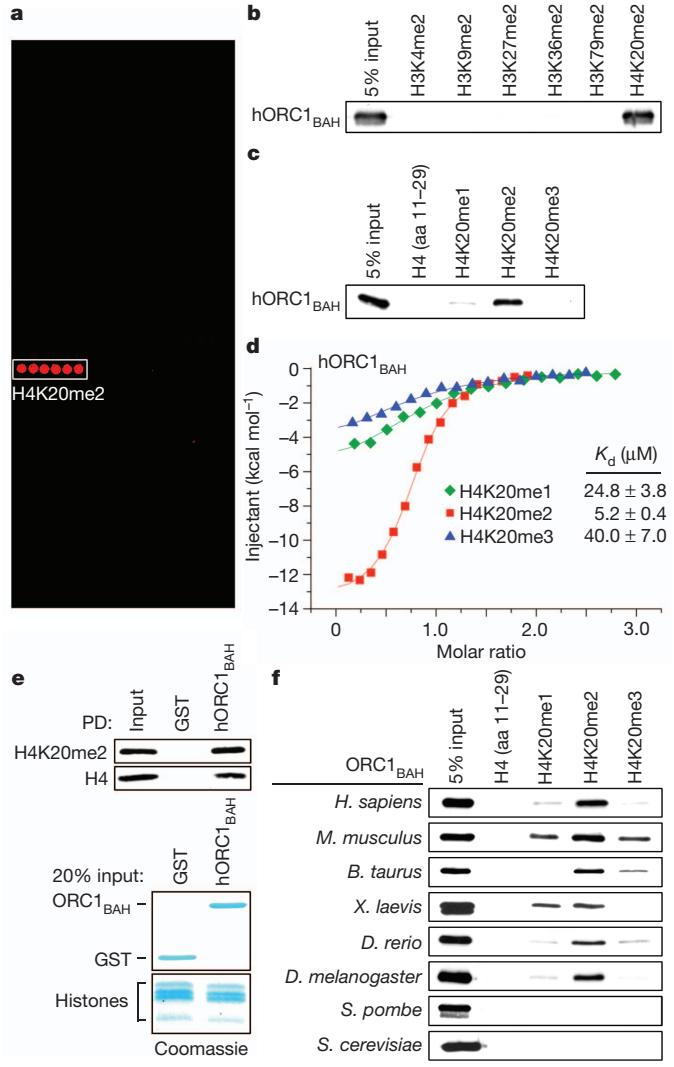

Figure 1 | The ORC1 BAH domain is a novel H4K20me2-binding module. **a**, hORC1$_{BAH}$ preferentially binds H4K20me2 peptides. Microarrays spotted with 82 distinct histone peptides as indicated in Supplementary Fig. 1 were probed with glutathione *S*-transferase (GST) fused to hORC1$_{BAH}$. Red spots indicate positive binding. **b**, **c**, hORC1$_{BAH}$ specifically binds H4K20me2 peptides. Western blot analysis of histone peptide pull-downs with GST–hORC1$_{BAH}$ and the indicated biotinylated peptides. aa, amino acids. **d**, hORC1$_{BAH}$ binds with highest affinity to H4K20me2. ITC was used to determine the K_d values for the interaction of hORC1$_{BAH}$ with the indicated peptides: H4K20me1 (green diamonds), H4K20me2 (red squares) and H4K20me3 (blue triangles). Standard deviation (s.d.) was derived from nonlinear fitting. **e**, hORC1$_{BAH}$ binds full-length H4K20me2. Top, western blot of GST–hORC1$_{BAH}$ and GST control pull-downs from calf thymus histones (CTH) with the indicated antibodies. Bottom, Coomassie blue stain of input (20% of total). PD, GST pull-downs. **f**, H4K20me2 binding is a common property of ORC1 BAH domains from diverse metazoan species. Binding assays as in **b** with GST-fused ORC1 BAH domains from the indicated species and using the indicated peptides.

hydrogen-bonding interactions involving Lys 16, His 18, Val 21 and Arg 23 of the bound peptide and residues lining the peptide-binding channel of mORC1$_{BAH}$ (Fig. 2b, c). Although backbone–backbone interactions represent the majority of contacts, a water-mediated hydrogen bond involving the imidazole ring of His 18, as well as a salt bridge between Lys 16 of the H4 peptide and Glu 126 of mORC1$_{BAH}$, are also observed (Fig. 2b, c). In this regard, acetylation at K16 slightly reduced the binding affinity of hORC1$_{BAH}$ and mORC1$_{BAH}$ for the H4K16acK20me2 peptide (Supplementary Fig. 4).

To investigate the structural dynamics of H4K20me2 binding, we determined the 1.70 Å crystal structure of mORC1$_{BAH}$ in the free state (crystallization statistics in Supplementary Table 1). Superimposition of the mORC1$_{BAH}$ structures in the free and peptide-bound states demonstrated that, although the interaction with H4K20me2 does not alter the conformation for the majority of the protein, the K20me2-binding pocket of mORC1$_{BAH}$ undergoes a significant rearrangement upon complex formation (Fig. 2e and Supplementary Fig. 5). Specifically, formation of the mORC1$_{BAH}$–H4K20me2 complex prompts the indole ring of Trp 119, which in the free state stacks with the indole ring of Trp 87, to swing aside and accommodate insertion of H4K20me2 (Fig. 2e). In addition, the interaction elicits reorientation of Glu 93 to allow its side chain to hydrogen bond with the methylammonium proton of H4K20me2 (Fig. 2e).

ITC studies establish that mORC1$_{BAH}$ binds to H4K20me2 peptide with a K_d of 9.6 μM, with the binding affinity towards H4K20me1 and H4K20me3 weaker by a factor of 2 to 3 (K_d = 32.7 μM and 17.4 μM, respectively; Supplementary Fig. 6a). The mORC1$_{BAH}$ domain shows moderate sequence conservation through evolution, with relatively high conservation of residues lining the H4K20me2-binding pocket (Supplementary Fig. 6b); hORC1$_{BAH}$ retains all the aromatic cage residues that recognize H4K20me2, except for Trp 119 of mORC1$_{BAH}$, which is substituted by Cys 120 in hORC1$_{BAH}$. Replacing mORC1$_{BAH}$ Trp 119 with a cysteine (human counterpart) resulted in increased discrimination of H4K20me2 over H4K20me3 from twofold to threefold, approaching the eightfold discrimination observed for hORC1$_{BAH}$ (Supplementary Fig. 6a). However, given that this mutant could not fully recapitulate the H4K20me2-binding specificity of hORC1$_{BAH}$ (Supplementary Fig. 6a), other residues probably contribute to H4K20me2 discrimination. Indeed, a C120A substitution in hORC1$_{BAH}$ decreases binding to all three methylation states of H4K20me, with retention of H4K20me2 specificity (Supplementary Fig. 6a).

ITC analysis also demonstrated that alanine substitutions of the remaining residues lining the H4K20me2-binding pocket of hORC1$_{BAH}$ (Y64A, W88A, E94A and Y115A) abolished or largely diminished H4K20me2 recognition (Fig. 2f). Similar results were observed with hORC1$_{BAH}$ and mORC1$_{BAH}$ cage mutants in peptide-binding assays (Fig. 2g and Supplementary Fig. 6c) and in histone-binding assays (Fig. 2h). These results further support the structural analysis and establish the molecular basis for the H4K20me2–ORC1$_{BAH}$ interaction.

H4K20me2 is an abundant H4 modification[18], and the BAH domain of ORC1, although dispensable for ORC complex assembly, has been shown to be important for loading of the complex onto chromatin in humans cells[19]. We therefore postulated that the interaction between ORC1 and H4K20me2 might regulate ORC stabilization at chromatin. First, ORC components (ORC2, ORC3 and ORC5) affinity purified with two structure-guided H4K20me2-binding mutants (hORC1(Y64A) and hORC1(W88A)) with an efficiency equal to that observed with the wild-type protein in both U2OS (Fig. 3a) and HT1080 (Supplementary Fig. 7a) human cell lines, suggesting that H4K20me2 binding by ORC1 is dispensable for ORC complex assembly. Next, analysis of lysates biochemically separated into chromatin-enriched and soluble fractions from cells stably expressing hORC1, hORC1(Y64A) or hORC1(W88A) demonstrated that hORC1(Y64A) and hORC1(W88A) enrichment at chromatin was considerably reduced in comparison to hORC1 (Fig. 3b and Supplementary Fig. 7b). Moreover, chromatin association of the ORC components ORC2, ORC3, ORC5 and ORC6 was compromised in cells expressing the ORC1 H4K20me2-binding-pocket mutants (Fig. 3c and Supplementary Fig. 7c). Thus, hORC1$_{BAH}$ binding to H4K20me2 is required for efficient stabilization of ORC1 and other ORC components at chromatin.

Local chromatin structure is thought to have a role in the mechanism that determines metazoan origins of replication[13]. In this context, chromatin immunoprecipitation (ChIP) assays with a highly specific H4K20me2 antibody in G1-synchronized U2OS cells (Supplementary Figs 8 and 9) demonstrated an increase in the H4K20me2 signal at two defined human replication origins[20–23] relative to adjacent

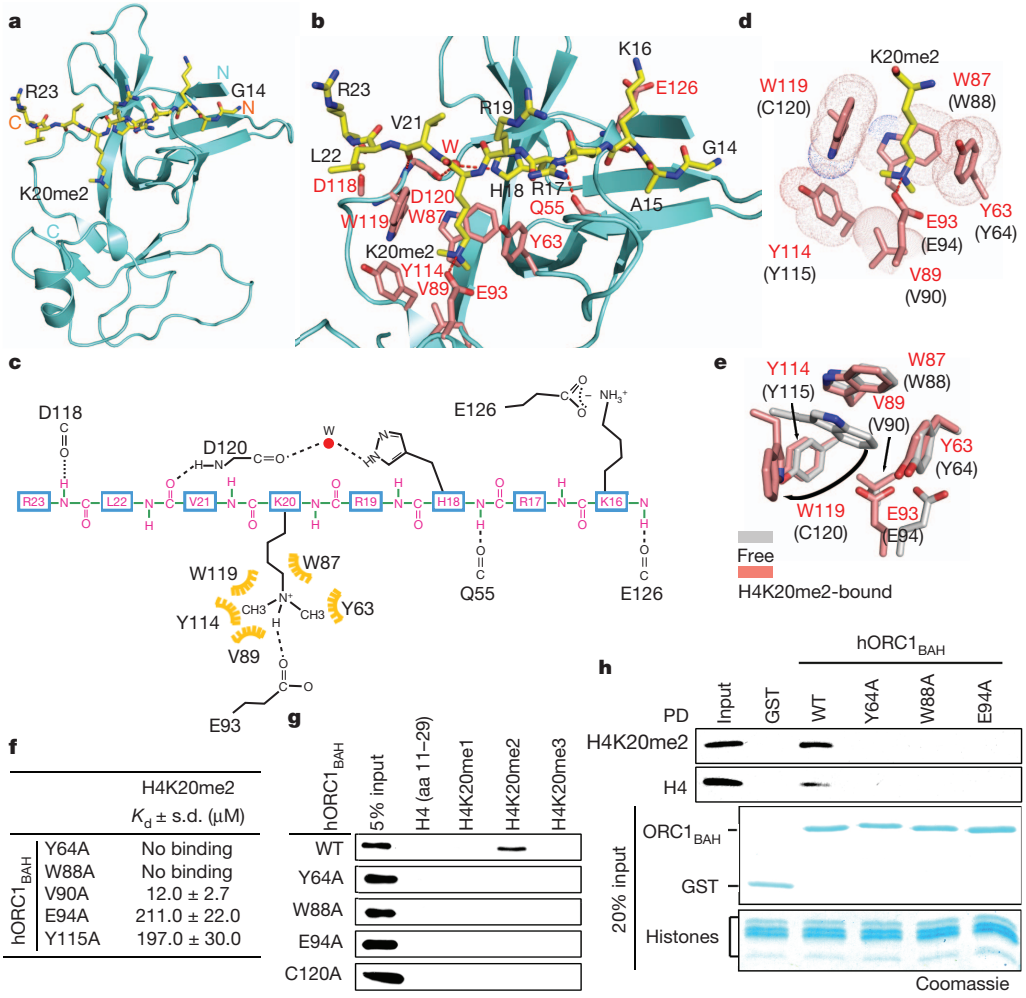

Figure 2 | The molecular basis of H4K20me2 recognition by ORC1$_{BAH}$. **a**–**c**, 1.95 Å crystal structure of mORC1$_{BAH}$ complexed with H4(14–25)K20me2 peptide. **a**, Ribbon representation of mORC1$_{BAH}$ bound to H4K20me2 peptide. The mORC1$_{BAH}$ (cyan) and the bound H4K20me2 peptide (yellow) are shown in ribbon and stick representations, respectively. **b**, Details of intermolecular contacts in the mORC1$_{BAH}$–H4K20me2 complex. mORC1$_{BAH}$ and H4K20me2 peptide residues are coloured in pink and yellow, respectively, with hydrogen bonds depicted as red dashed lines, and a water molecule (W) as a red sphere. **c**, Schematic representation of intermolecular contacts in the mORC1$_{BAH}$–H4K20me2 complex. The residues from the H4K20me2 peptide and mORC1$_{BAH}$ are coloured in magenta and black, respectively. Yellow indicates the hydrophobic contact. **d**, Positioning of the K20me2 side chain within an aromatic cage of the indicated residues (red) on the surface of mORC1$_{BAH}$. The equivalent cage residues in hORC1$_{BAH}$ are labelled in parentheses. **e**, Structural overlay of the mORC1$_{BAH}$ K20me2-binding aromatic cage in the free (silver) and H4K20me2-bound states (salmon). The curved arrow indicates binding-induced structural shift. **f**, Mutations in the hORC1$_{BAH}$ H4K20me2-binding channel impair H4K20me2 recognition. ITC analysis of the indicated hORC1$_{BAH}$ mutants binding to H4K20me2 peptide; s.d. derived from nonlinear fitting. **g**, **h**, Mutations in the hORC1$_{BAH}$ dimethyl-lysine-binding cage abrogate H4K20me2 recognition. **g**, Binding assays as in Fig. 1b with the indicated hORC1$_{BAH}$ mutant proteins and biotinylated peptides. **h**, Top, western blot analysis of CTH-binding assays as in Fig. 1e with the indicated proteins and antibodies. PD, GST pull-downs. Bottom, Coomassie blue stain of input GST-fusion proteins and histones (20% of total). WT, wild type.

sequences (Fig. 3d and Supplementary Fig. 10). Moreover, like the pattern of H4K20me2, hORC1 occupancy peaked at origins relative to adjacent sequences (Fig. 3e and Supplementary Fig. 10). In contrast, hORC1(Y64A) and hORC1(W88A) enrichment at origins was not observed, even though the H4K20me2 peak at origins is present in these cell lines (Figs 3d, e and Supplementary Fig. 10). These data suggest that H4K20me2 may have a role at human origins by stabilizing ORC1 at chromatin.

ORC marks genomic origins of replication during the G1 phase of the cell cycle and serves to nucleate assembly of the pre-DNA replication complex (pre-RC) to coordinate DNA replication during S phase[14]. As a core component of this licensing machinery, ORC1 is required for efficient cell-cycle progression and the transition from G1 to S phase[4,19]. In this context, cell-cycle analysis demonstrated a decreased S-phase population and a lower S/G1 ratio in WI-38 primary fibroblasts transiently expressing the H4K20me2-binding mutants hORC1(Y64A) and hORC1(W88A) relative to wild-type hORC1-overexpressing cells (Fig. 3f). Notably, mouse embryonic fibroblasts isolated from mice lacking the enzymes that generate H4K20me2 (Suv420h1 and Suv420h2) show DNA replication defects, including delayed S-phase entry[18]. Thus, ORC1 recognition of the canonical H4K20me2 mark appears to facilitate ORC chromatin loading to promote DNA replication and cell-cycle progression.

Mutations in components of the pre-DNA replication machinery, including ORC1, have recently been identified in individuals with MGS and, in a zebrafish model, *orc1* morphants display an MGS-like proportionate dwarfism phenotype[3,4,24]. In MGS individuals, the majority of *ORC1* mutations fall within the protein's BAH domain[3,4], including two mutants (F89S and E127G) that are in regions that impinge upon H4K20me2 recognition (Fig. 4a) and decrease binding of hORC1$_{BAH}$ to H4K20me2 peptides (Fig. 4b, c). Furthermore, mice deficient in H4K20me2 synthesis are born significantly smaller than control littermates[18]. Together, these observations implicate disruption of the ORC1–H4K20me2 interaction in MGS pathogenesis. To

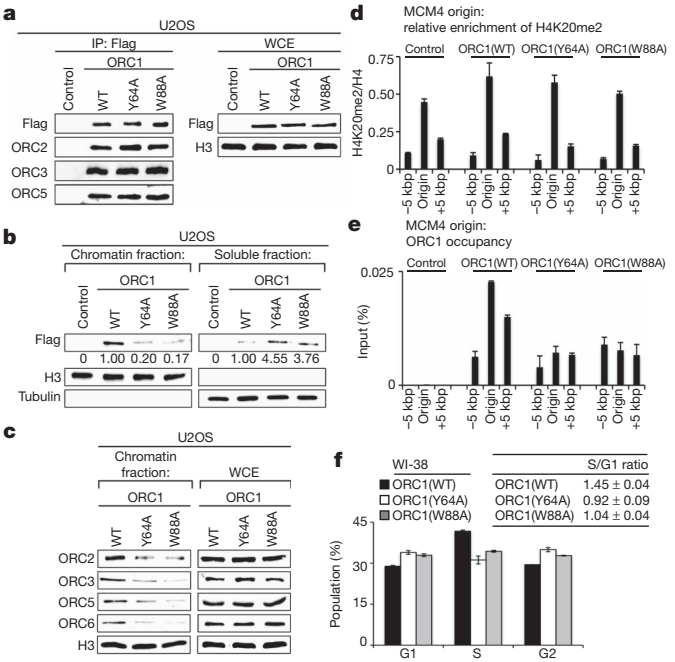

Figure 3 | ORC1–H4K20me2 interaction regulates ORC chromatin association and cell-cycle progression. **a**, Western blot analysis with the indicated antibodies of wild-type (WT) and H4K20me2-binding-pocket mutants (Y64A and W88A) affinity-purified Flag-tagged ORC1 complexes from U2OS cells. Control, empty vector control immunoprecipitate (IP). WCE, whole cell extract. **b**, The $ORC1_{BAH}$–H4K20me2 interaction is required for efficient ORC1 chromatin association. Western blot analysis of lysates biochemically separated into chromatin-enriched and soluble fractions from U2OS cells stably expressing the indicated ORC1 protein. Quantification of Flag–ORC1 levels is shown. Control, empty vector control lysates. Tubulin and H3 levels are shown as control for the integrity of fractionation. **c**, Disruption of ORC1 binding to H4K20me2 destabilizes ORC chromatin association. Western blot analysis of biochemically purified chromatin from U2OS cells as in **b** with the indicated antibodies. Total ORC protein levels in WCE are shown. **d**, H4K20me2 is enriched at DNA replication origins. H4K20me2 signal normalized to total H4 at the MCM4 origin and indicated flanking regions in G1-phase-synchronized U2OS cells stably expressing the indicated ORC protein; *y*-axis shows H4K20me2 ChIP/H4 ChIP. **e**, An intact BAH domain is required for ORC1 occupancy at replication origins. Occupancy of Flag-tagged hORC1, hORC1(Y64A), hORC1(W88A) or control was determined by ChIP analysis (*y*-axis shows percentage input) as in **d**. Error bars in **d** and **e** indicate s.e.m. from three experiments. **f**, The ORC1–H4K20me2 interaction is required for efficient cell-cycle progression. The cell-cycle profile of WI-38 cells transiently expressing GFP and the indicated ORC1 protein was determined by flow cytometry. GFP-positive cells were used to ensure that only transfected cells were analysed. Left, percentage of cells in the indicated cell-cycle phase is shown. Right, the S/G1 ratio for the indicated transfections is shown. Error bars indicate s.d. from two experiments.

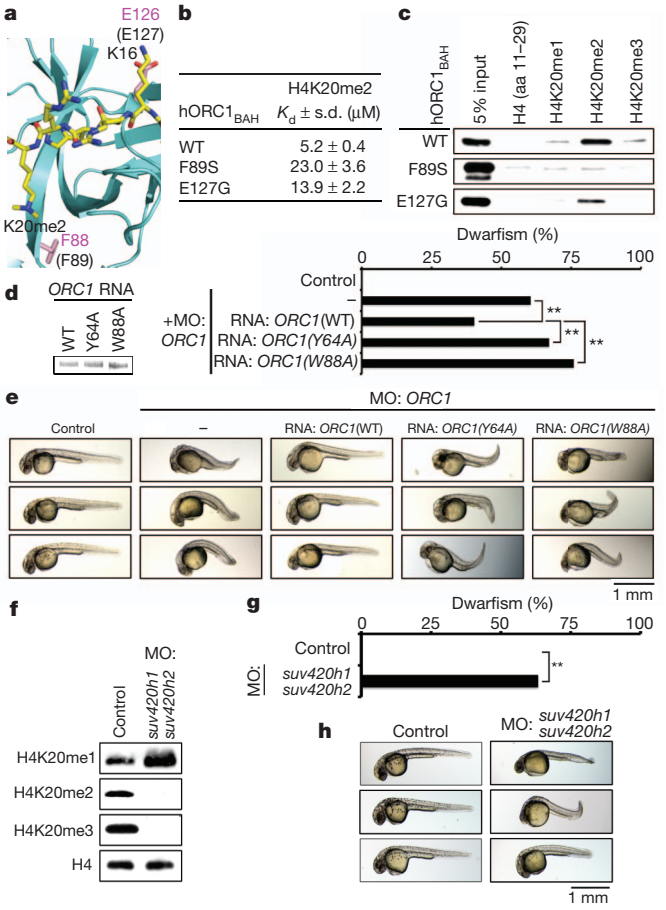

Figure 4 | Disruption of the $ORC1_{BAH}$–H4K20me2 interaction leads to dwarfism in zebrafish. **a**–**c**, MGS-associated mutations F89S and E127G impair H4K20me2 binding by hORC1. **a**, Close-up view of $mORC1_{BAH}$ bound to H4K20me2, with residues F88 and E126 (equivalent to F89 and E127 in hORC1, respectively) shown in stick representation. **b**, ITC analysis as in Fig. 1d of F89S and E127G $hORC1_{BAH}$ mutants binding to H4K20me2 peptides. ITC data for wild-type $hORC1_{BAH}$ from Fig. 1d. **c**, Binding assays as in Fig. 1b with the indicated $hORC1_{BAH}$ mutant proteins and biotinylated peptides. **d**, **e**, The H4K20me2-recognition activity of hORC1 is required to rescue the dwarfism phenotype of *orc1* morphants. **d**, Quantification of dwarf phenotype in zebrafish injected with MOs targeting the *orc1* translation start site alone or MO co-injected with the indicated h*ORC1* mRNAs. Insert on left shows electrophoresis analysis of the indicated h*ORC1* mRNAs used for reconstitution. Control, uninjected embryos. Dwarfism was defined as a reduction of body length of ≥3 s.d. relative to the average size of the control zebrafish. Zebrafish analysed: control, 26; *orc1* MO, 86; MO + h*ORC1* wild type, 67; MO + h*ORC1(Y64A)*, 85; MO + h*ORC1(W88A)*, 83. *P* values are calculated with a two-tailed unpaired Student's *t*-test. $^{**}P < 0.01$. **e**, Representative images of zebrafish in **d** 1 day post-fertilization (dpf). **f**, Depletion of H4K20me2/3 in *suv420h1/suv420h2* morphants. Western blot analysis using the indicated antibodies of whole animal extracts 1 dpf from control zebrafish or zebrafish injected with MOs targeting the translation start sites of *suv420h1* and *suv420h2*. Control, uninjected embryos. **g**, **h**, Dwarfism in *suv420h1/suv420h2* morphants. **g**, Quantification of dwarfism in *suv420h1/suv420h2* morphants relative to controls as described in **d**. Zebrafish analysed: control, 38; MO, 60. $^{**}P < 0.01$. **h**, Representative images of zebrafish in **g** 1 dpf.

test this hypothesis, an *orc1* zebrafish morphant reconstitution system was established. Injection of two independent *orc1*-targeting morpholino oligonucleotides (MOs) resulted in growth retardation, recapitulating published results[4] (Fig. 4d, e and data not shown). Co-injection of human *ORC1* messsenger RNA with zebrafish *orc1*-targeting MOs attenuated the dwarf phenotype observed in the *orc1* morphant alone (Fig. 4d, e). In contrast, co-injection of h*ORC1(Y64A)* and h*ORC1(W88A)* mRNA failed to rescue *orc1* morphants, moderately aggravating the growth retardation phenotype (Fig. 4d, e).

The H4K20me2/3 lysine methyltransferases (KMTs) Suv420h1 and Suv420h2 are conserved in zebrafish[25]. As shown in Fig. 4f, injection of MOs targeting *Danio rerio suv420h1* and *suv420h2* resulted in global depletion of H4K20me2 and H4K20me3, and an increase in H4K20me1; these changes in H4K20 methylation are similar to those observed in cells derived from *Suv420h1/20h2* double-knockout mice[18]. Analysis of body size in the *suv420h1/20h2* morphants demonstrated that H4K20me2 depletion results in a significant dwarfism phenotype compared to controls (Fig. 4g, h). Finally, *orc1/suv420h1/20h2* morphants did not display significantly more dwarfisms than *orc1* or *suv420h1/20h2* morphants (Supplementary Fig. 11). Together, these data indicate that the specific recognition of H4K20me2 by the BAH domain of ORC1 has a crucial role in determining organism body size.

We have identified the BAH domain as a novel methyl-lysine-binding module, demonstrating that H4K20me2 recognition is an evolutionarily conserved function for BAH domains from diverse

metazoan ORC1 proteins. To our knowledge, these results provide the first direct link between histone methylation and the metazoan DNA replication machinery. The mechanism that determines metazoan origins of replication is thought to be dependent upon both the information encoded in the DNA sequence at origins, as well as the local chromatin architecture[13,14]. Several histone modifications have been detected at origins[20–22,26,27], including H3K27me1, which regulates replication of DNA at heterochromatin in *Arabidopsis*[28]. The mark H4K20me1 is present in early G1 at human origins and probably serves as the chromatin template for H4K20me2 catalysis[18,29,30]. Because H4K20me1 is generated in a highly cell-cycle-regulated manner by the KMT PR-Set7 (also known as SET8), this modification may regulate licensing by governing the temporal and spatial availability of H4K20me2 at origins[29]. We postulate that the recognition of H4K20me2 by ORC1 cooperates with other ORC chromatin-loading mechanisms in marking replication origins. On the basis of this model, during developmental phases requiring rapid cell division, inefficient pre-RC formation due to abrogation of the ORC1–H4K20me2 interaction would result in delayed cell-cycle progression and insufficient cellular proliferation, a characteristic of proportional 'hypocellular' dwarfism disorders like MGS[5]. Together, our findings reveal a new function for histone methylation signalling at chromatin in the regulation of DNA replication and organismal growth.

METHODS SUMMARY

Materials, peptide microarray experiments, binding assays, structure analysis and crystallization conditions, and zebrafish experiments and data analysis are described in detail in Methods. For the zebrafish experiments, wild-type AB zebrafish (*D. rerio*) were maintained and raised using standard protocols. All zebrafish were treated in accordance with AAALAC approved guidelines at Stanford University (protocol number 10511).

Full Methods and any associated references are available in the online version of the paper at www.nature.com/nature.

Received 24 November 2011; accepted 17 February 2012.
Published online 7 March 2012.

1. Taverna, S. D., Li, H., Ruthenburg, A. J., Allis, C. D. & Patel, D. J. How chromatin-binding modules interpret histone modifications: lessons from professional pocket pickers. *Nature Struct. Mol. Biol.* **14,** 1025–1040 (2007).
2. Duncker, B. P., Chesnokov, I. N. & McConkey, B. J. The origin recognition complex protein family. *Genome Biol.* **10,** 214 (2009).
3. Bicknell, L. S. *et al.* Mutations in the pre-replication complex cause Meier-Gorlin syndrome. *Nature Genet.* **43,** 356–359 (2011).
4. Bicknell, L. S. *et al.* Mutations in ORC1, encoding the largest subunit of the origin recognition complex, cause microcephalic primordial dwarfism resembling Meier-Gorlin syndrome. *Nature Genet.* **43,** 350–355 (2011).
5. Klingseisen, A. & Jackson, A. P. Mechanisms and pathways of growth failure in primordial dwarfism. *Genes Dev.* **25,** 2011–2024 (2011).
6. Kouzarides, T. Chromatin modifications and their function. *Cell* **128,** 693–705 (2007).
7. Callebaut, I., Courvalin, J. C. & Mornon, J. P. The BAH (bromo-adjacent homology) domain: a link between DNA methylation, replication and transcriptional regulation. *FEBS Lett.* **446,** 189–193 (1999).
8. Onishi, M., Liou, G. G., Buchberger, J. R., Walz, T. & Moazed, D. Role of the conserved Sir3-BAH domain in nucleosome binding and silent chromatin assembly. *Mol. Cell* **28,** 1015–1028 (2007).
9. Sampath, V. *et al.* Mutational analysis of the Sir3 BAH domain reveals multiple points of interaction with nucleosomes. *Mol. Cell. Biol.* **29,** 2532–2545 (2009).
10. Armache, K. J., Garlick, J. D., Canzio, D., Narlikar, G. J. & Kingston, R. E. Structural basis of silencing: Sir3 BAH domain in complex with a nucleosome at 3.0 Å resolution. *Science* **334,** 977–982 (2011).
11. Bua, D. J. *et al.* Epigenome microarray platform for proteome-wide dissection of chromatin-signaling networks. *PLoS ONE* **4,** e6789 (2009).
12. Bell, S. P., Mitchell, J., Leber, J., Kobayashi, R. & Stillman, B. The multidomain structure of Orc1p reveals similarity to regulators of DNA replication and transcriptional silencing. *Cell* **83,** 563–568 (1995).
13. Dorn, E. S. & Cook, J. G. Nucleosomes in the neighborhood: new roles for chromatin modifications in replication origin control. *Epigenetics* **6,** 552–559 (2011).
14. Bell, S. P. & Dutta, A. DNA replication in eukaryotic cells. *Annu. Rev. Biochem.* **71,** 333–374 (2002).
15. Zhang, Z., Hayashi, M. K., Merkel, O., Stillman, B. & Xu, R. M. Structure and function of the BAH-containing domain of Orc1p in epigenetic silencing. *EMBO J.* **21,** 4600–4611 (2002).
16. Botuyan, M. V. *et al.* Structural basis for the methylation state-specific recognition of histone H4-K20 by 53BP1 and Crb2 in DNA repair. *Cell* **127,** 1361–1373 (2006).
17. Li, H. *et al.* Structural basis for lower lysine methylation state-specific readout by MBT repeats of L3MBTL1 and an engineered PHD finger. *Mol. Cell* **28,** 677–691 (2007).
18. Schotta, G. *et al.* A chromatin-wide transition to H4K20 monomethylation impairs genome integrity and programmed DNA rearrangements in the mouse. *Genes Dev.* **22,** 2048–2061 (2008).
19. Noguchi, K., Vassilev, A., Ghosh, S., Yates, J. L. & DePamphilis, M. L. The BAH domain facilitates the ability of human Orc1 protein to activate replication origins *in vivo*. *EMBO J.* **25,** 5372–5382 (2006).
20. Tardat, M. *et al.* The histone H4 Lys 20 methyltransferase PR-Set7 regulates replication origins in mammalian cells. *Nature Cell Biol.* **12,** 1086–1093 (2010).
21. Tardat, M., Murr, R., Herceg, Z., Sardet, C. & Julien, E. PR-Set7-dependent lysine methylation ensures genome replication and stability through S phase. *J. Cell Biol.* **179,** 1413–1426 (2007).
22. Miotto, B. & Struhl, K. HBO1 histone acetylase is a coactivator of the replication licensing factor Cdt1. *Genes Dev.* **22,** 2633–2638 (2008).
23. Kitsberg, D., Selig, S., Keshet, I. & Cedar, H. Replication structure of the human β-globin gene domain. *Nature* **366,** 588–590 (1993).
24. Guernsey, D. L. *et al.* Mutations in origin recognition complex gene *ORC4* cause Meier-Gorlin syndrome. *Nature Genet.* **43,** 360–364 (2011).
25. Sun, X. J. *et al.* Genome-wide survey and developmental expression mapping of zebrafish SET domain-containing genes. *PLoS ONE* **3,** e1499 (2008).
26. Costas, C. *et al.* Genome-wide mapping of *Arabidopsis thaliana* origins of DNA replication and their associated epigenetic marks. *Nature Struct. Mol. Biol.* **18,** 395–400 (2011).
27. Miotto, B. & Struhl, K. HBO1 histone acetylase activity is essential for DNA replication licensing and inhibited by Geminin. *Mol. Cell* **37,** 57–66 (2010).
28. Jacob, Y. *et al.* Regulation of heterochromatic DNA replication by histone H3 lysine 27 methyltransferases. *Nature* **466,** 987–991 (2010).
29. Brustel, J., Tardat, M., Kirsh, O., Grimaud, C. & Julien, E. Coupling mitosis to DNA replication: the emerging role of the histone H4-lysine 20 methyltransferase PR-Set7. *Trends Cell Biol.* **21,** 452–460 (2011).
30. Oda, H. *et al.* Monomethylation of histone H4-lysine 20 is involved in chromosome structure and stability and is essential for mouse development. *Mol. Cell. Biol.* **29,** 2278–2295 (2009).

Supplementary Information is linked to the online version of the paper at www.nature.com/nature.

Acknowledgements We thank R. Tennen for critical reading of the manuscript. This work was supported in part by grants to O.G. (R01 GM079641), D.J.P. (Abby Rockefeller Mauze, STARR and Maloris Foundations) and J.K.C. (DP1 OD003792), and a predoctoral fellowship to A.J.K. (Genentech Foundation). O.G. is a recipient of an Ellison Senior Scholar in Aging Award.

Author Contributions A.J.K. and P.C. performed the molecular biology, cellular and zebrafish studies; J.S. performed structural and binding affinity studies; S.Y. and J.K.C. advised on zebrafish experiments; S.I.-M. assisted in protein production and crystallization. A.J.K., P.C., J.S., D.J.P. and O.G. designed studies, analysed data and wrote the paper. All authors discussed and commented on the manuscript.

Author Information Atomic coordinates have been deposited with the Protein Data Bank under accession codes 4DOV (free structure) and 4DOW (H4K20me2-bound $mORC1_{BAH}$) for the reported crystal structures. Reprints and permissions information is available at www.nature.com/reprints. The authors declare no competing financial interests. Readers are welcome to comment on the online version of this article at www.nature.com/nature. Correspondence and requests for materials should be addressed to D.J.P. (pateld@mskcc.org) or O.G. (ogozani@stanford.edu).

METHODS

Materials and plasmids. Biotinylated peptides were synthesized at Stanford or Yale Protein and Nucleic Acid facilities as previously described[11]. Antibodies used in this study: anti-histone H3 (Abcam), anti-Flag M5 (Sigma), anti-GST (Abcam), anti-tubulin (Upstate), anti-ORC2 (Upstate), anti-ORC3 (Abcam), anti-ORC5 (Sigma), anti-ORC6 (Abcam), anti-H4 (Abcam), anti-H4K20me1 (Abcam), anti-H4K20me2 (Abcam), anti-H4K20me3 (Abcam). ORC1 BAH domain was cloned into pGEX6P-1 for *in vitro* binding experiments, pBABE-puro-3×Flag for generating cell lines stably expressing ORC1 proteins, pCDNA-HA-EGFP and pCAG-Flag ORC1 for transfection in WI-38 cells, pcDNA for producing *in vitro*-transcribed mRNA for zebrafish microinjection. Site-directed mutagenesis was performed to introduce point mutations (Stratagene).

Cell culture, cell synchronization and transfection. 293T, HT1080 and U2OS cells were cultured in DMEM (Invitrogen) supplemented with 10% fetal bovine serum (ATCC), glutamine (Invitrogen) and penicillin/streptomycin (Invitrogen). U2OS cells were synchronized in 0.1 μg ml^{-1} nocodazole (Sigma) for 24 h. Cells were collected for ChIP analysis and flow cytometry 6 h after releasing with DMEM. WI-38 human primary fibroblasts were maintained in DMEM/F12 (Invitrogen) with added supplements. Transient transfection was performed using TransIT-LT1 or TransIT-293 (Mirus) following the manufacturer's protocol.

Flow cytometry. Cells were collected and fixed in 70% ethanol at −20 °C for 15 min and rehydrated in PBS for 15 min. Cells were then stained with 3 μM propidium iodide and 10 μg ml^{-1} Rnase A (Sigma) in staining buffer (100 mM Tris, pH 7.4, 150 mM NaCl, 1 mM $CaCl_2$, 0.5 mM $MgCl_2$, 0.1% NP-40) for 30 min.

Modified histone peptide microarrays. Peptide microarray experiments were performed as described previously[11]. Briefly, biotinylated histone peptides diluted in phosphate-buffered saline (PBS) supplied with 5% glycerol and 0.05% Tween-20 were printed on streptavidin-coated glass slides (ArrayIt) using VersArray Compact Microarrayer (BioRad). The arrays were probed with 25 μg of GST–$ORC1_{BAH}$ and protein–peptide interactions were detected using anti-GST antibodies (Abcam) followed by Alexa Fluor 647 chicken anti-rabbit IgG antibodies (Invitrogen). To validate the epitope-specificity of H4K20me2 antibodies, the arrays were probed with 1 μg of the indicated antibodies and the epitope-antibody bindings were detected by the same fluorophore-conjugated antibody as described above.

Biotinylated peptide binding assay. Biotinylated peptide pull-down assay was previously described[31]. Briefly, 1 μg of peptide was incubated with 1 μg of recombinant proteins in the binding buffer containing 50 mM Tris, pH 7.5, 150 mM NaCl and 0.05% NP-40. Peptides were pulled down using streptavidin sepharose beads (Amersham) and protein–peptide bindings were detected by western analyses.

Full-length histone binding assay. Full-length histone pull-down assays were performed as previously described[32]. Briefly, 5 μg of full-length histones purified from calf thymus (Wormington) was incubated with 25 μg of recombinant proteins in the binding solution containing 50 mM Tris, pH 7.5, 150 mM NaCl and 0.05% NP-40. Recombinant proteins were pulled down using glutathione sepharose 4B beads (Amersham) and bound histones were detected by western blot analysis.

Protein expression and purification for structure analyses. For structure determination, the gene encoding residues 9–170 of mouse ORC1 was PCR amplified and inserted into a modified pRSFDuet-1 vector (Novagen), in which $mORC1_{BAH}$ was separated from the preceding His_6-SUMO tag by a ubiquitin-like protease (ULP1) cleavage site. The fusion protein was expressed in BL21 (DE3) RIL cell strain (Stratagene), in LB medium or minimum medium supplemented with 70 mg l^{-1} seleno-methionine for selenium labelling. The cells were grown at 37 °C and induced by 0.4 mM isopropyl β-D-1-thiogalactopyranoside (IPTG) when $OD_{600\,nm}$ reached approximately 0.6. The temperature was then shifted to 20 °C for overnight culture growth. The fusion protein was purified through a Ni-NTA affinity column. The His_6-SUMO tag was removed by ULP1 cleavage, followed by a second round of Ni-NTA column purification, and gel filtration on a 16/60 G200 Superdex column. The final sample for crystallization of the $mORC1_{BAH}$ domain contains about 10 mg ml^{-1} $mORC1_{BAH}$ domain, 20 mM Tris-HCl, 50 mM NaCl, 5 mM DTT, pH 7.5.

For mutational analysis, mutants of the BAH domain human ORC1(1–185) were constructed by direct mutagenesis and purified as described above.

Crystallization conditions. For crystallization, the $mORC1_{BAH}$ domain was mixed with H4(14–25)K20me2 peptide in a molar ratio of 1:4. The crystallization condition (0.2 M sodium bromide, 25% PEG3350, 20 °C) was initially identified using sparse-matrix screens (Hampton Research). The crystals were subsequently reproduced and improved by the hanging-drop vapour-diffusion method, from drops mixed from 1 μl of H4K20me2–$mORC1_{BAH}$ domain solution and 1 μl of precipitant solution. This crystallization condition, when further supplemented with 0.2 M 3-(1-pyridino)-1-propane sulphonate (Hampton Research), led to production of the crystals of free $mORC1_{BAH}$, even though the H4(14–25)K20me2 peptide was present in the crystallization solution. The crystals for both free and H4(14–25)K20me2-bound $mORC1_{BAH}$ domain were soaked in cryoprotectant made of mother liquor supplemented with 25% glycerol, before flash freezing in liquid nitrogen.

Structure determination. X-ray diffraction data sets for both free and H4(14–25)K20me2-bound $mORC1_{BAH}$ domain were collected at selenium peak wavelength on the 24-IDE NE-CAT beamline at the Advanced Photo Source, Argonne National Laboratory. The diffraction data were indexed, integrated and scaled using the HKL 2000 program. The structure of free $mORC1_{BAH}$ was solved by the single-wavelength dispersion method with selenium atoms using the AutoSol program embedded in PHENIX software[33], which also gave an initial structural model. Further modelling of $mORC1_{BAH}$ domain was carried out using COOT[34], and was then subject to refinement using PHENIX. The final model was refined to 1.70 Å resolution.

The structure of H4K20me2(14–25)-bound $mORC1_{BAH}$ domain was solved by the molecular replacement method in PHASER[35] using the free structure of the $mORC1_{BAH}$ domain as a search model. The H4(14–25)K20me2 peptide was then modelled in COOT and the structure of the H4(14–25)K20me2-$mORC1_{BAH}$ domain was refined using PHENIX. The final model of the complex was refined to 1.95 Å resolution. For both free and H4(14–25)K20me2-$mORC1_{BAH}$ domain structures, the *B* factors were refined with individual *B* values.

The statistics for data collection and structural refinement for both free and H4(14–25)K20me2-bound $mORC1_{BAH}$ domain are summarized in Supplementary Table 1.

ITC measurements. Protein and peptide samples used for ITC measurements were subject to overnight dialysis against buffer containing 20 mM Tris-HCl, 100 mM NaCl, 2 mM DTT, pH 7.5. Before the measurement, the protein and peptide concentrations were adjusted to about 0.1 mM and 1 mM, respectively. The ITC experiment was carried out using a MicroCal iTC200 instrument at 5 °C. The titration curves were analysed using software Origin7.0 (MicroCal, iTC200).

Small-scale biochemical fractionation. Small-scale biochemical fractionation was modified from a protocol described previously[36]. In short, 1×10^7 to 2×10^7 U2OS and HT1080 cells were collected, washed with PBS, and resuspended in buffer A (10 mM HEPES, pH 7.9, 10 mM KCl, 1.5 mM $MgCl_2$, 0.34 M sucrose, 10% glycerol, 1 mM DTT, complete protease inhibitor tablet (Roche)). Trition X-100 was added to a final concentration of 0.1%. Cells were incubated for 8 min, and nuclei were collected by centrifugation (1,300*g*, 4 °C, 5 min). The supernatant (S1) was clarified by centrifugation at 20,000*g*, 4 °C for 5 min. The nuclei were washed once with buffer A and lysed in buffer B (3 mM EDTA, 0.2 mM EGTA, 1 mM DTT, complete protease inhibitor tablet) for 30 min. Chromatin was collected by centrifugation (1,700*g*, 4 °C, 5 min). The soluble fraction was combined with S1 and boiled at 90 °C with SDS sample buffer. Chromatin was washed with buffer B once and resuspended in SDS sample buffer, boiled at 90 °C for 10 min.

Immunoprecipitation. HT1080 and U2OS cells stably expressing Flag–ORC1 or Flag–ORC1 mutants were generated by retroviral transduction. Cells were lysed in cell lysis buffer containing 50 mM Tris-HCl, pH 7.4, 250 mM NaCl, 0.5% Triton X-100, 10% glycerol, 1 mM DTT, complete protease inhibitor tablet (Roche). Flag–ORC1 complexes were affinity purified by incubating anti-Flag m2 monoclonal-antibody-conjugated agarose beads (Sigma) in lysates overnight at 4 °C. Flag M2 beads were then washed three times with cell lysis buffer and bound protein eluted in SDS buffer for western blot analysis.

ChIP analysis. ChIP was performed as previously described[37]. The primer sequences used in this study were: MCM4, −5 kbp forward, TTCACATCCA CCCAGCTTATC; MCM4, −5 kbp reverse, AGAGCATTCTTCCCCTGATG; MCM4 origin, reverse, TTGGGTGGCTACTTGGTGTT; MCM4 origin, reverse, TAGGCCCCTCGCTTGTTT; MCM4, +5 kbp forward, TTTTGAATCTT GGTTTTGCTGA; MCM4, +5 kbp reverse, CAGCTTTTGGTTGGCTAAGG; β-globin, −40 kbp forward, AGGTCAGGCCCTCAAGAGTC; β-globin, −40 kbp reverse, CAGTCAGTTCTTTGGACAAGTCTTA; β-globin origin, forward, TGAGCCTCTGCTGATTCATTT; β-globin origin, reverse, TTCAAGGGAGAG ACCTCATTGT; β-globin, +70 kbp forward, CTCAGAAGAACCCTTGAT CTCC; β-globin, +70 kbp reverse, TTCCGAGGACATTGGTTGA.

Zebrafish aquaculture and microinjection. Wild-type AB zebrafish (*D. rerio*) were maintained and raised using standard protocols. All experiments were conducted in accordance with AAALAC approved guidelines at Stanford University (protocol number 10511). Embryos obtained from natural matings were microinjected at the 1-to-2-cell stage with 1.5 nl of 0.18 mM sequence-specific *orc1* morpholino or 0.36 mM *suv420h1/h2* combined morpholinos at 1:1 ratio targeting each gene's translation start site (GeneTools). For epistasis analyses, 1.5 nl of morpholino solution containing 0.18 mM *orc1* morpholino and 0.36 mM *suv420h1/h2* combined morpholino (1:1 ratio) was used for microinjection. *orc1*, TCAGTCTTGTGATGTAGCGGCTCAT (described in ref. 4); *suv420h1*, ACCATGTTCTTGGATTCTCCCATCT; *suv420h2*, CACTCATTCTATAAGAT CCCTCCAT. The morpholino targeting the *orc1* splice-site junction: ACAA CTCTATTATGCTCACCTGTAC, as previously described[4]. For reconstitution

experiments, capped full-length ORC1 wild-type or H4K20me2-binding-pocket mutant mRNAs were transcribed *in vitro* following the manufacturer's manual (Ambion). Ten picograms of mRNA was co-microinjected with *orc1* morpholino at the 1-cell stage. Embryos were cultured in E3 medium at 28.5 °C for 24 h before scoring phenotypes. Live fish images were captured for individual fish using a Leica M205FA stereomicroscope and body length was calculated by Leica Application Suite program. Percentage of dwarf fish (average for control − 3× standard deviation of control) in each experiment group was scored and *P* values between groups were calculated by unpaired two-tailed Student's *t*-test.

31. Shi, X. *et al.* ING2 PHD domain links histone H3 lysine 4 methylation to active gene repression. *Nature* **442,** 96–99 (2006).
32. Matthews, A. G. *et al.* RAG2 PHD finger couples histone H3 lysine 4 trimethylation with V(D)J recombination. *Nature* **450,** 1106–1110 (2007).
33. Adams, P. D. *et al.* PHENIX: building new software for automated crystallographic structure determination. *Acta Crystallogr. D* **58,** 1948–1954 (2002).
34. Emsley, P. & Cowtan, K. Coot: model-building tools for molecular graphics. *Acta Crystallogr. D* **60,** 2126–2132 (2004).
35. McCoy, A. J. *et al.* Phaser crystallographic software. *J. Appl. Cryst.* **40,** 658–674 (2007).
36. Mendez, J. & Stillman, B. Chromatin association of human origin recognition complex, Cdc6, and minichromosome maintenance proteins during the cell cycle: assembly of prereplication complexes in late mitosis. *Mol. Cell. Biol.* **20,** 8602–8612 (2000).
37. Kuo, A. J. *et al.* NSD2 links dimethylation of histone H3 at lysine 36 to oncogenic programming. *Mol. Cell* **44,** 609–620 (2011).

doi:10.1038/nature10956

a

b

X	=	X X X X X X
H4 (aa 1-23)	H3 (aa 21-44)	H2A (aa 1-21)
H4K5me1	H3K27me1	H2AK5Ac
H4K5me2	H3K27me2	H2AK13Ac
H4K5me3	H3K27me3	
H4 (aa 1-23)	H3 (aa 21-44)	H2B (aa 1-21)
H4K8me1	H3K36me1	H2BK5me1
H4K8me2	H3K36me2	H2BK5me2
H4K8me3	H3K36me3	H2BK5me3
H4 (aa 1-23)	H3 (aa 67-89)	H2BK5Ac
H4K12me1	H3K79me1	H2BK12Ac
H4K12me2	H3K79me2	H2BK15Ac
H4K12me3	H3K79me3	H2BK20Ac
H4 (aa 1-23)	H3 (aa 1-21)	H3 (aa 1-21)
H4K5/8/12me1	H3R2me1	H3K4me1
H4K5/8/12me2	H3R2(s)me2	H3K4me2
H4K5/8/12me3	H3R2(a)me2	H3K4me3
H4 (aa 11-29)	H3 (aa 1-21)	H3 (aa 1-21)
H4K20me1	H3R17me1	H3K9me1
H4K20me2	H3R17(s)me2	H3K9me2
H4K20me3	H3R17(a)me2	H3K9me3
H4 (aa 1-23)	H3 (aa 21-44)	H3 (aa 1-21)
H4R3me1	H3R26me1	H3K14me1
H4R3(s)me2	H3R26(s)me2	H3K14me2
H4R3(a)me2	H3R26(a)me2	H3K14me3
H4K5Ac	H3R2Cit	H3 (aa 10-27)
H4K8Ac	H3R17Cit	H3K18me1
H4K12Ac	H3R26Cit	H3K18me2
H4K16Ac	H4R3Cit	H3K18me3
H2AX(121-142)	H3K9Ac	H3 (aa 21-44)
H2AXS139ph	H3K18Ac	H3K23me1
	H3T3ph	H3K23me2
	H3S10ph	H3K23me3

c

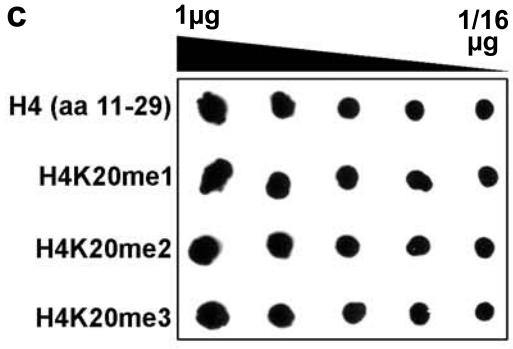

Supplementary Figure 1. hORC1$_{BAH}$ preferentially binds H4K20me2. a, Independent replica of data in Figure 1a, showing hORC1$_{BAH}$ preferential binding to H4K20me2 on peptide microarrays. **b**, Schematic of the histone peptides spotted on the histone peptide microarrays. **c**, The indicated biotinylated histone peptides used in peptide pull-down assays (Fig. 1c, 1f, 2g, and 4c) were spotted onto nitrocellulose membrane in serial dilution and detected with streptavidin-HRP.

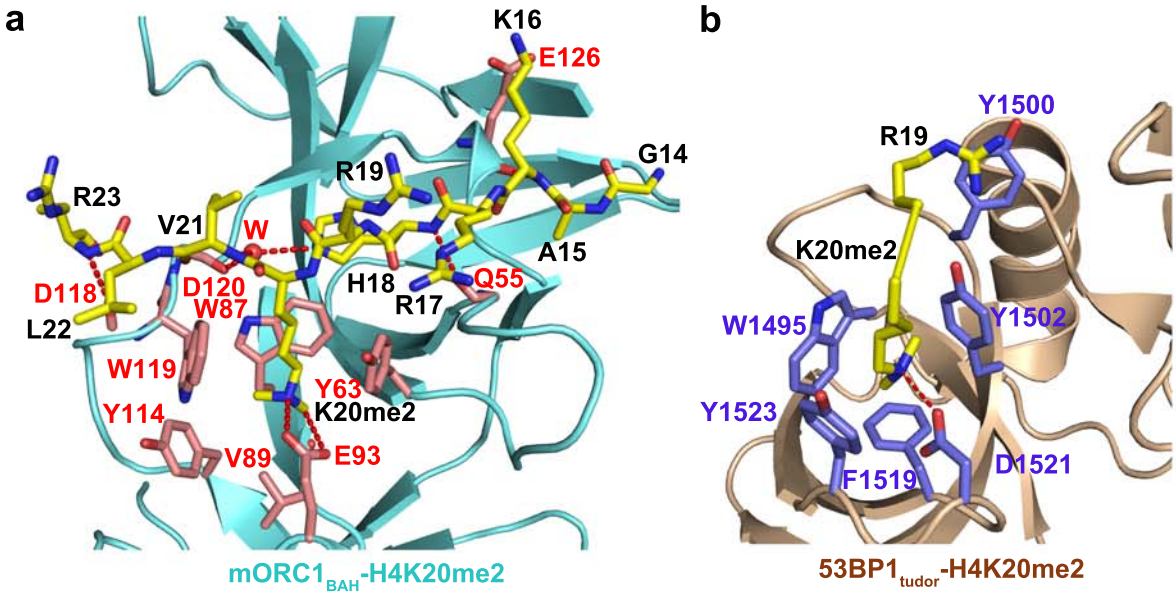

Supplementary Figure 2. Comparison of intermolecular contacts between mORC1$_{BAH}$-H4K20me2 and 53BP1 tudor domain (53BP1$_{tudor}$)-H4K20me2 complexes. **a**, Details of intermolecular contacts in the mORC1$_{BAH}$-H4K20me2 complex, the same as shown in Fig. 2b. **b**, Details of intermolecular contacts in the 53BP1$_{tudor}$-H4K20me2 complex (PDB 2IG0). 53BP1$_{tudor}$ and H4K20me2 peptide residues are colored in blue and yellow, respectively, with hydrogen bonds depicted as red dashed lines. Structural comparison of these two complexes indicates that both mORC1$_{BAH}$ and 53BP1$_{tudor}$ adopt an aromatic cage, adjoined by an acidic residue, to specifically recognize the H4K20me2 mark. However, the two proteins engage in distinct sequence specific interactions with the H4K20me2 peptide. In the mORC1$_{BAH}$-H4K20me2 complex, a fragment encompassing residues 16-23 of H4 is involved in intermolecular contacts with mORC1$_{BAH}$. By contrast, only residues H4R19 and H4K20me2 appear to interact with 53BP1$_{tudor}$ in the 53BP1$_{tudor}$-H4K20me2 complex. Notably, residue H4R19 associates with Tyr1500 of 53BP1$_{tudor}$ through a cation-π interaction in the latter complex, unlike that in the mORC1$_{BAH}$-H4K20me2 complex where its side chain is left exposed to the solvent.

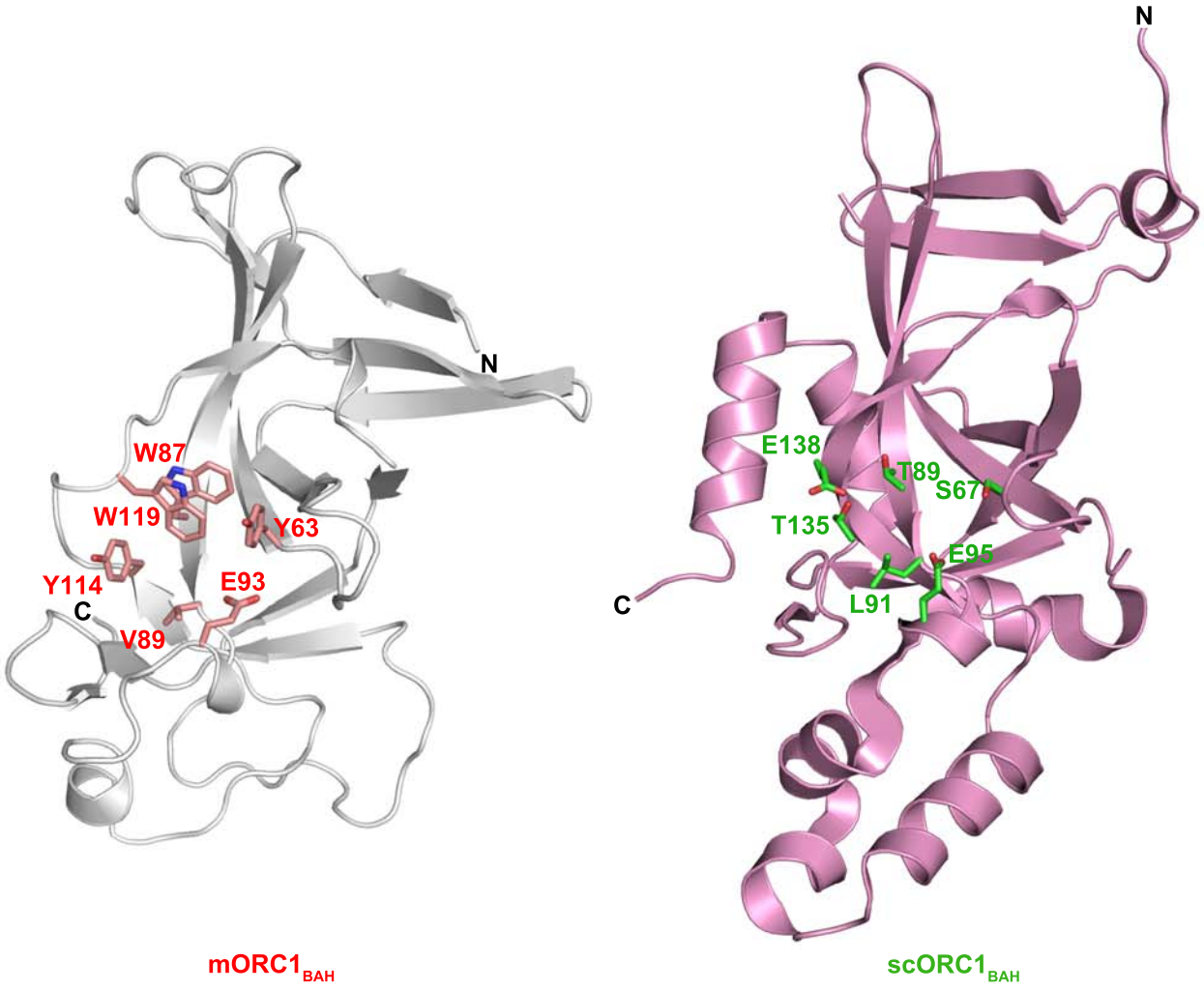

Supplementary Figure 3. Structural comparison of $mORC1_{BAH}$ and $scORC1_{BAH}$. The residues lining the H4K20me2-binding cage of $mORC1_{BAH}$ are colored in pink, and the residues in the corresponding positions in $scORC1_{BAH}$ are colored in green. Comparison of these two structures indicates that $scORC1_{BAH}$ does not form an aromatic cage to harbor H4K20me2, explaining why $scORC1_{BAH}$ is incapable of binding to H4K20me2.

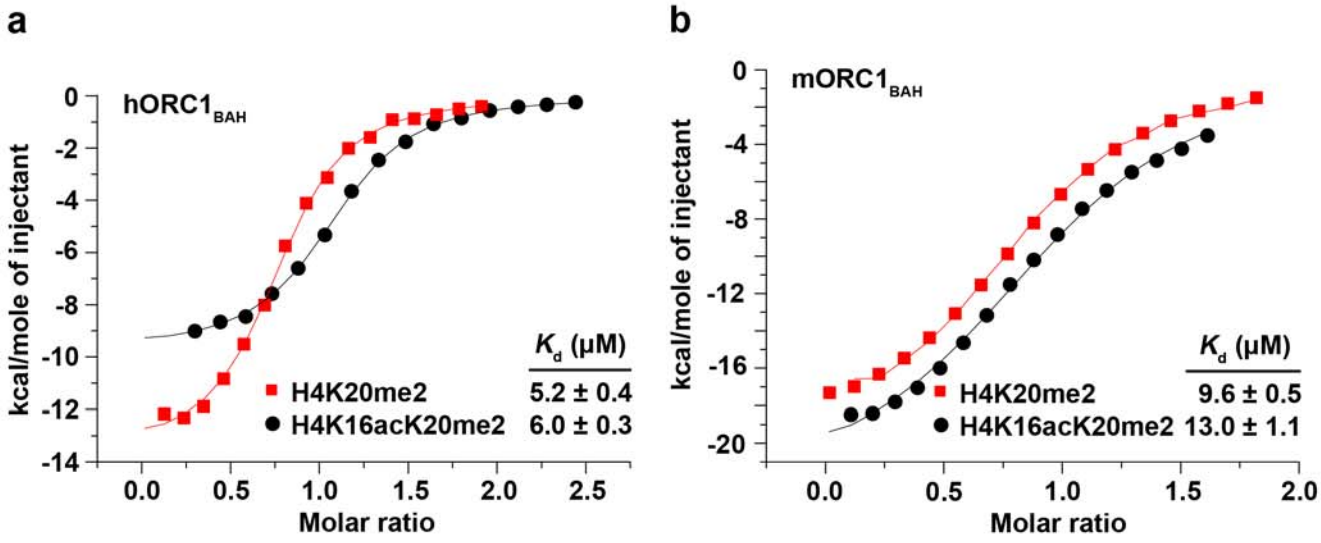

Supplementary Figure 4. Impact of H4K16 acetylation on h(m)ORC1$_{BAH}$-H4K20me2 interaction. **a**, ITC analysis of the interactions of hORC1$_{BAH}$ with H4K20me2 (red squares) and H4K20me2 acetylated at H4K16 (H4K16acK20me2, black circles) peptides. The ITC data for wild-type hORC1$_{BAH}$ is reproduced from Fig. 1d. **b**, ITC analysis of the interactions of mORC1$_{BAH}$ with H4K20me2 (red squares) and H4K16acK20me2 (black circles) peptides. These results indicate that acetylation of H4K16 resulted in slightly weaker binding (higher K_d values) for both hORC1$_{BAH}$-H4K20me2 and mORC1$_{BAH}$-H4K20me2 complexes.

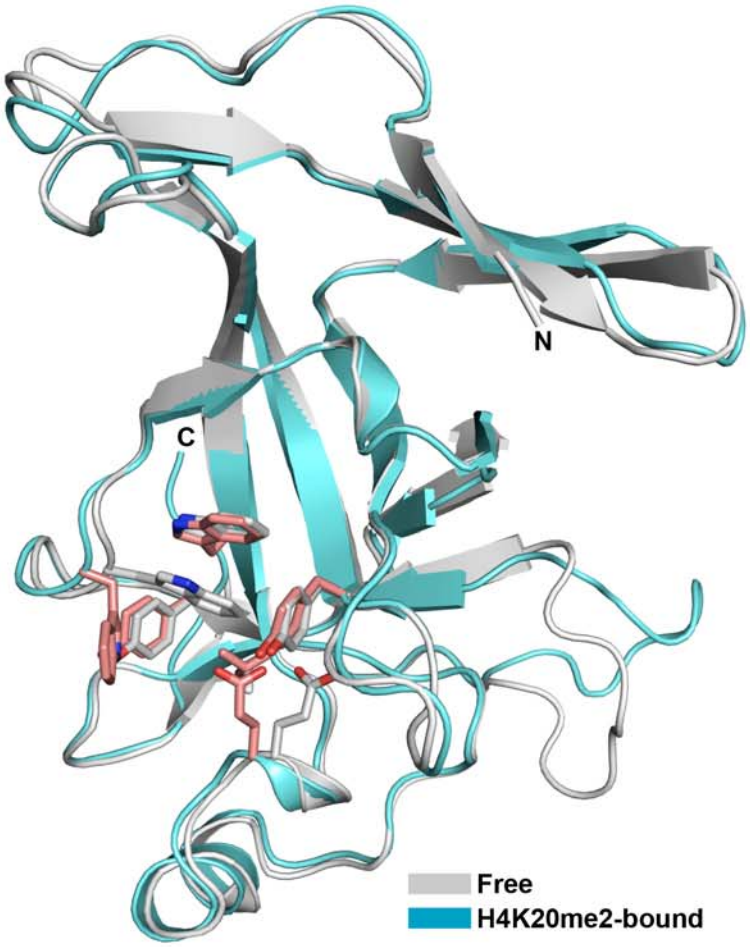

Supplementary Figure 5. The structural overly between free and H4(14-25)K20me2-bound mORC1$_{BAH}$ domains. The residues forming the H4K20me2-binding pocket are shown in stick representation, colored silver in free state and salmon in the H4K20me2-bound state.

a

Peptide	K_d ± s.d. (μM)			
	Wild-type $mORC1_{BAH}$	W119C $mORC1_{BAH}$	Wild-type $hORC1_{BAH}$	C120A $hORC1_{BAH}$
H4K20me1	32.7 ± 1.4	40.5 ± 3.0	24.8 ± 3.8	308.0 ± 21.0
H4K20me2	9.6 ± 0.5	11.0 ± 1.2	5.2 ± 0.4	27.4 ± 4.4
H4K20me3	17.4 ± 0.9	32.3 ± 3.7	40.0 ± 7.0	319.0 ± 46.0

b

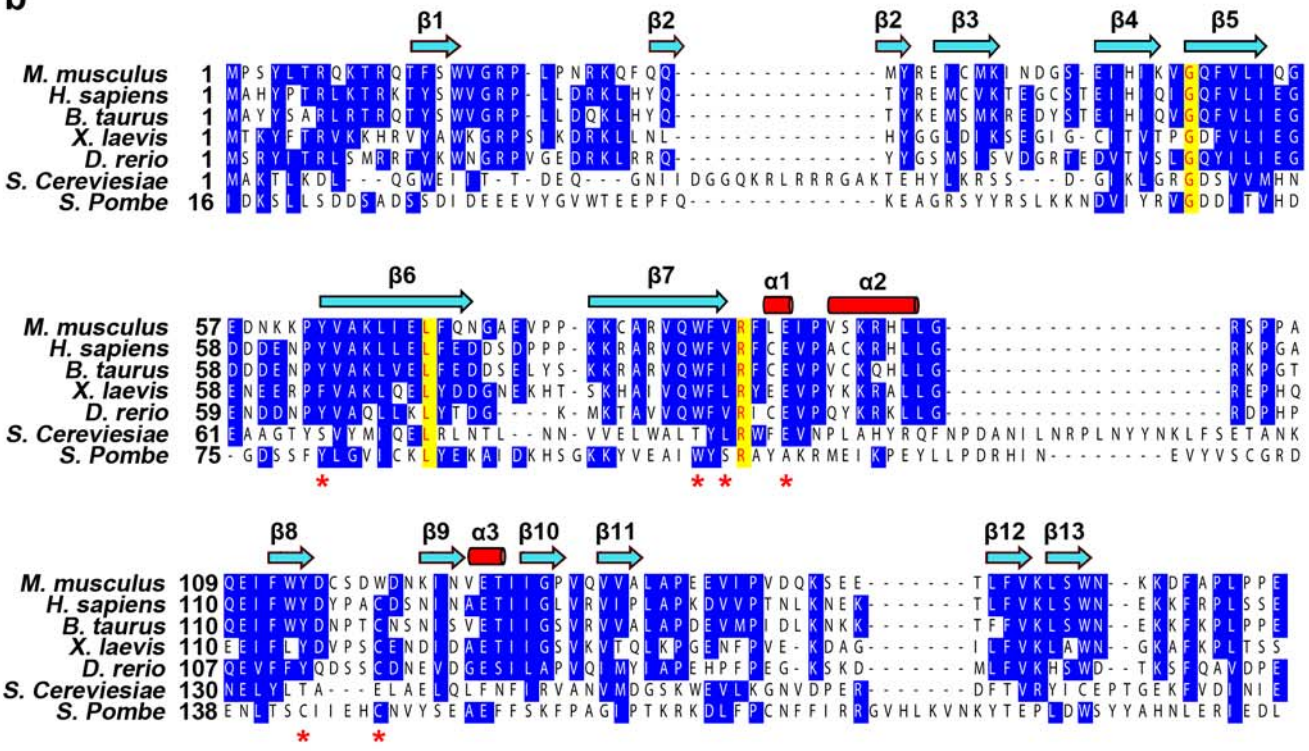

c

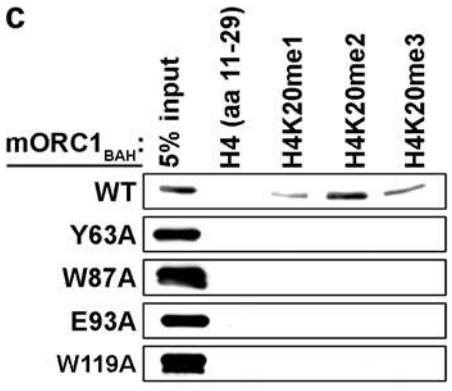

Supplementary Figure 6. Evolutionary conservation of the ORC1 BAH domain. **a**, Binding affinities of $mORC1_{BAH}$, $mORC1_{BAH}$ W119C mutant, $hORC1_{BAH}$ and $hORC1_{BAH}$ C120A mutant for the indicated H4K20 peptides determined by ITC as in (Fig. 1d). Note that replacement of Trp119 of $mORC1_{BAH}$ with a cysteine slightly improves its discrimination of H4K20me2 against H4K20me3. **b**, Sequence alignment of $ORC1_{BAH}$ for listed species using Clustal W. Completely conserved residues are colored in red and highlighted in yellow. Identical or similar residues are highlighted in blue. H4K20me2-binding residues are indicated with a red asterisk (*). Note that these residues are not well conserved in $scORC1_{BAH}$ and $spORC1_{BAH}$. α, alpha-helix. β, beta-sheet. **c**, Peptide-binding assays of $mORC1_{BAH}$ mutants with the indicated peptides.

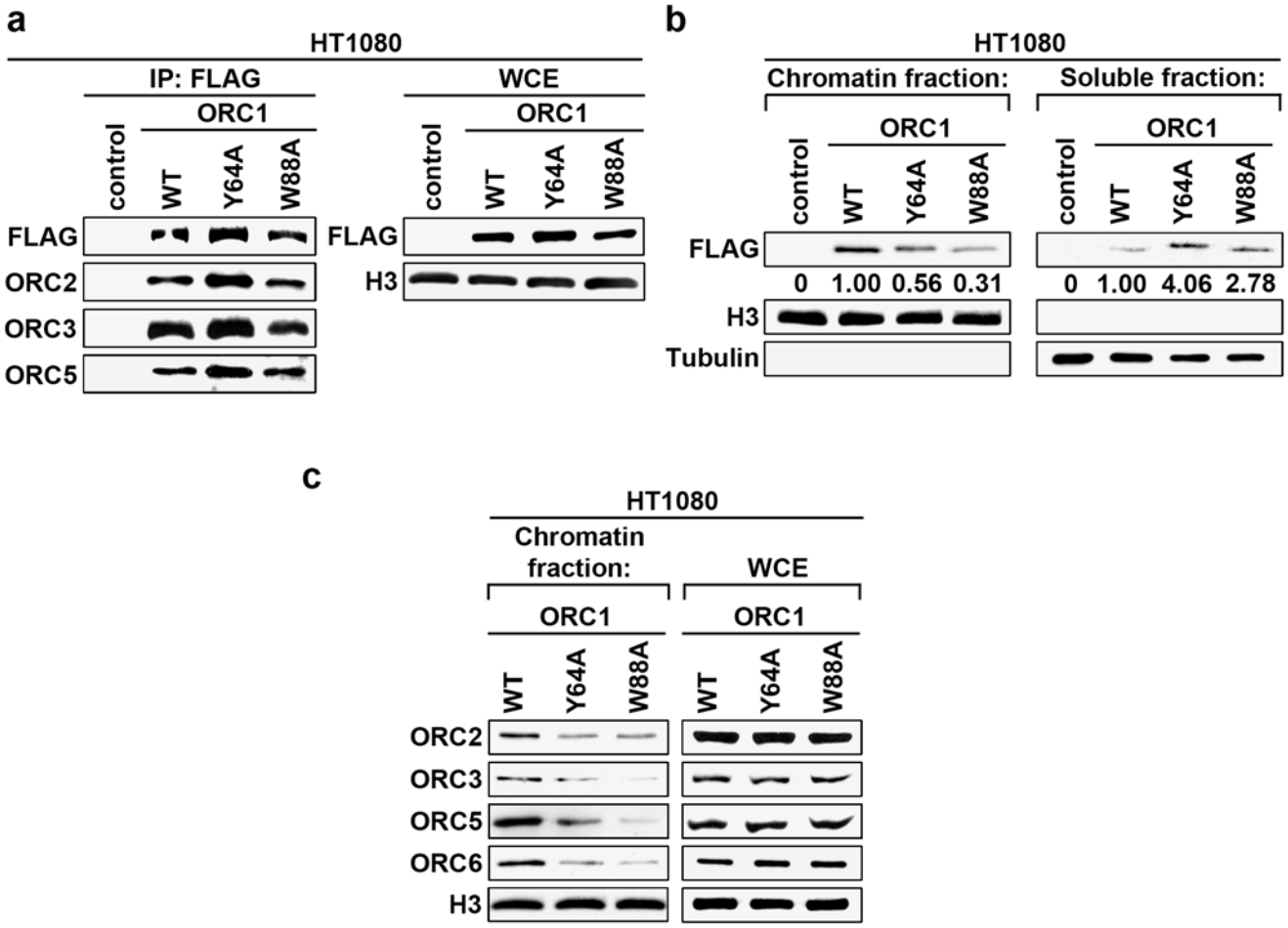

Supplementary Figure 7. ORC1-H4K20me2 interaction regulates ORC chromatin association. a, Western blot analysis with the indicated antibodies of wild-type (WT) and H4K20me2-binding pocket mutants (Y64A and W88A) affinity-purified FLAG-tagged ORC1 complexes from HT1080 cells. Control, empty vector control IP. WCE, whole cell extract. **b,** The $ORC1_{BAH}$-H4K20me2 interaction is required for efficient ORC1 chromatin association. Western blot analysis of lysates biochemically separated into chromatin-enriched and soluble fractions from HT1080 cells stably expressing the indicated ORC1 protein. Quantitation of FLAG-ORC1 levels is shown. Control, empty vector control lysates. Tubulin and H3 levels are shown as control for the integrity of fractionation. **c,** Disruption of ORC1 binding to H4K20me2 destabilizes ORC chromatin association. Western blot analysis of biochemically purified chromatin from HT1080 cells as in (b) with the indicated antibodies. Total ORC protein levels in WCE are shown.

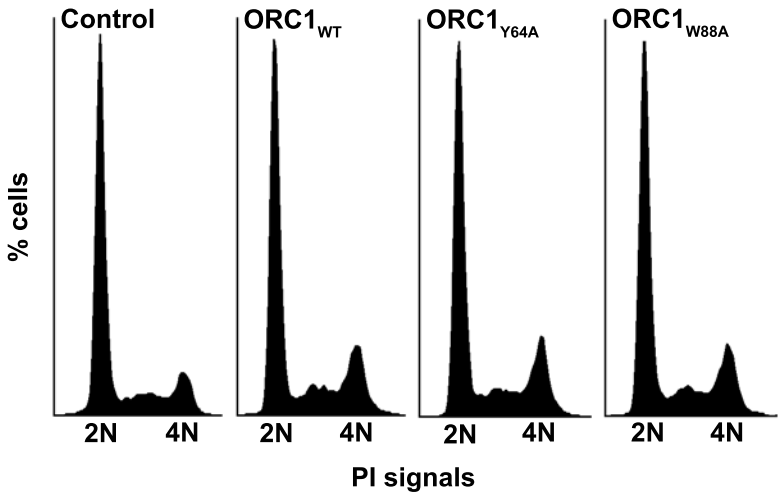

Supplementary Figure 8. Flow cytometry analysis of U2OS cells synchronized in G1 phase of the cell cycle. U2OS cells stably expressed the indicated ORC1 protein used for the experiments in Figure 3d and 3e were synchronized in M-phase with nocodazole and released into G1-phase (see Methods). The cell-cycle profiles were determined by PI staining followed by flow cytometry.

X	=	X X X X X X
H4 (aa 1-23)	H3 (aa 21-44)	H2A (aa 1-21)
H4K5me1	H3K27me1	H2AK5Ac
H4K5me2	H3K27me2	H2AK13Ac
H4K5me3	H3K27me3	
H4 (aa 1-23)	H3 (aa 21-44)	H2B (aa 1-21)
H4K8me1	H3K36me1	H2BK5me1
H4K8me2	H3K36me2	H2BK5me2
H4K8me3	H3K36me3	H2BK5me3
H4 (aa 1-23)	H3 (aa 67-89)	H2BK5Ac
H4K12me1	H3K79me1	H2BK12Ac
H4K12me2	H3K79me2	H2BK15Ac
H4K12me3	H3K79me3	H2BK20Ac
H4 (aa 1-23)	H3 (aa 1-21)	H3 (aa 1-21)
H4K5/8/12me1	H3R2me1	H3K4me1
H4K5/8/12me2	H3R2(s)me2	H3K4me2
H4K5/8/12me3	H3R2(a)me2	H3K4me3
H4 (aa 11-29)	H3 (aa 1-21)	H3 (aa 1-21)
H4K20me1	H3R17me1	H3K9me1
H4K20me2	H3R17(s)me2	H3K9me2
H4K20me3	H3R17(a)me2	H3K9me3
H4 (aa 1-23)	H3 (aa 21-44)	H3 (aa 1-21)
H4R3me1	H3R26me1	H3K14me1
H4R3(s)me2	H3R26(s)me2	H3K14me2
H4R3(a)me2	H3R26(a)me2	H3K14me3
H4K5Ac	H3R2Cit	H3 (aa 10-27)
H4K8Ac	H3R17Cit	H3K18me1
H4K12Ac	H3R26Cit	H3K18me2
H4K16Ac	H4R3Cit	H3K18me3
H2AX(121-142)	H3K9Ac	H3 (aa 21-44)
H2AXS139ph	H3K18Ac	H3K23me1
	H3T3ph	H3K23me2
	H3S10ph	H3K23me3

Supplementary Figure 9. H4K20me2 antibody shows specific binding to H4K20me2 peptide. Peptide microarray analysis of H4K20me2 rabbit polyclonal antibody used for ChIP assays in Fig. 3d-e (left). Schematic of the histone peptides spotted on the histone peptide microarrays (right).

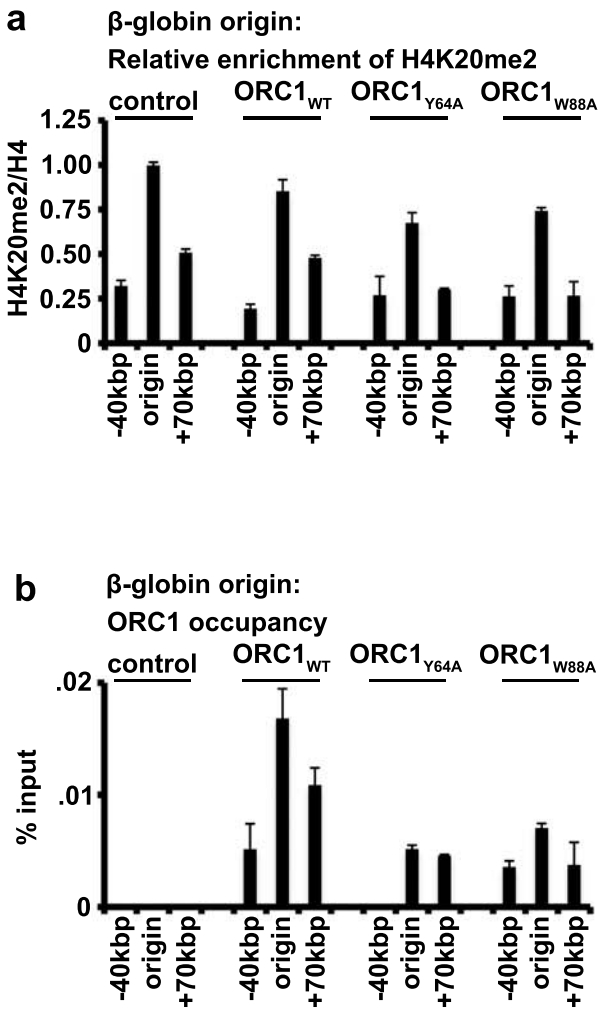

Supplementary Figure 10. H4K20me2 is enriched at DNA replication origins and an intact BAH domain is required for ORC1 occupancy at replication origins. a, ChIP analyses of H4K20me2 signals at the β-globin origins and the indicated flanking regions in G1 phase synchronized U2OS cells stably expressing the indicated ORC1 protein; *y*-axis: H4K20me2 ChIP/H4 ChIP. **b,** Occupancy of FLAG tagged hORC1, $hORC1_{Y64A}$, $hORC1_{W88A}$, or control was determined by ChIP analysis (*y*-axs: % input) at the indicated origins as in (a). Error bars in (a, and b,) indicate s.e.m. from three experiments.

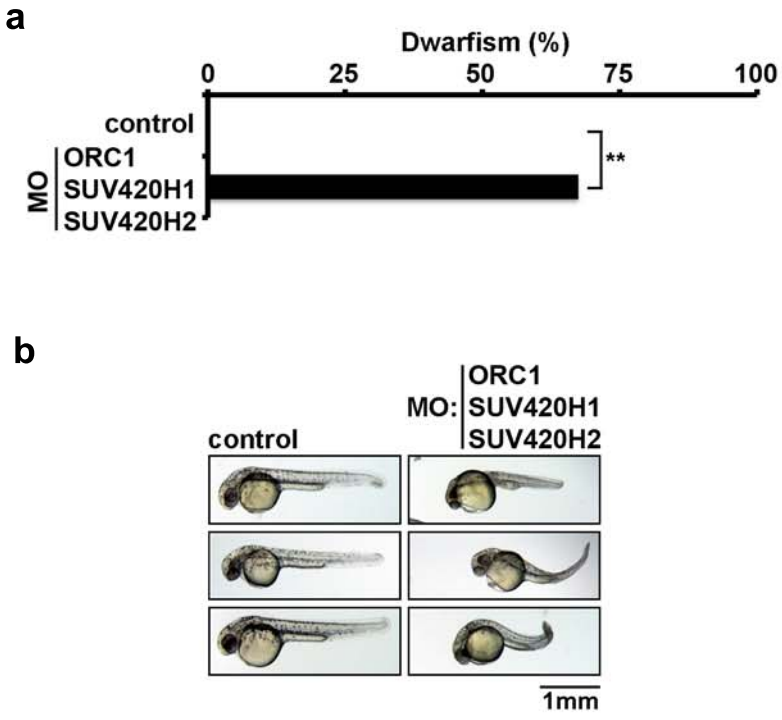

Supplementary Figure 11. *orc1/suv4-20h1/h2* morphants do not display significantly more dwarfism than *orc1* or *suv4-20h1/h2* morphants. a, Quantification of dwarf phenotype in zebrafish injected with morpholino oligos (MO) targeting the *Orc1*, *Suv4-20h1* and *Suv4-20h2* translation start sites as in Figure 4. Control, uninjected embryos. Zebrafish analyzed: control: 54; MO: 126. ** $P < 0.01$. **b**, representative images of zebrafish in (a) 1 day post-fertilization.

Supplementary Table 1. Crystallographic statistics for free and H4(14-25)K20me2-bound mORC1$_{BAH}$ domain.

	mORC1$_{BAH}$	**H4(14-25)K20me2-mORC1$_{BAH}$**
Data collection	**SeMet**	**Native**
Wavelength (Å)	0.9792	0.9792
Space group	*P21*	*P1*
Cell dimensions		
a, *b*, *c* (Å)	49.9, 53.9, 72.0	35.1, 49.4, 54.4
α, β, γ (°)	90, 102.4, 90	89.9, 102.1, 103.3
Resolution (Å)*	30-1.7 (1.76-1.70)	30-1.95 (2.02-1.95)
R_{sym} or R_{merge}*	6.4 (44.5)	6.8 (25.3)
$I/\sigma I$	24.3 (2.8)	12.3 (2.8)
Completeness (%)*	99.5 (100.0)	96.9 (95.8)
Redundancy*	3.7 (3.7)	2.1 (2.0)
Unique reflections	41,079 (4,090)	25,244 (2,482)
Refinement		
Resolution (Å)	22.4-1.7	25.9-1.95
No. reflections	41,016	24,544
R_{work}/ R_{free}	21.5/24.3	21.3/25.7
No. atoms		
Protein	2,467	2,490
Water	240	196
Peptide		386
B-factors		
Protein	30.3	40.9
Water	38.9	43.9
Peptide		47.2
R.m.s deviations		
Bond lengths (Å)	0.007	0.011
Bond angles (°)	1.120	1.408

*Highest resolution shell is shown in parenthesis.